Parameter Estimation in Layered Media Using Dispersion-Constrained Inversion

Hamidreza Mashayekh, S.M.ASCE[1]; Loukas F. Kallivokas, M.ASCE[2]; and John L. Tassoulas, M.ASCE[3]

Abstract: The need to estimate the properties of layered elastic or viscoelastic media arises commonly in various engineering applications, including geotechnical site characterization and pavement condition assessment. The layered medium is usually probed with small-amplitude waves, and the medium's response is used to drive an inverse medium problem leading to the identification of the properties. The property estimation problem is solved by a new methodology that seeks to minimize the misfit between measured and computed responses, constrained by the dispersion relation of the layered medium, the latter expressed in terms of the forward eigenvalue problem and the associated orthonormality condition. The medium's properties are recovered upon satisfaction of the first-order optimality conditions of the system's Lagrangian. The reported numerical results are based on synthetic records illustrating the methodology in the frequency domain, and demonstrating reconstruction of the medium's material properties and geometric characteristics. **DOI: 10.1061/(ASCE)EM.1943-7889.0001527.** © *2018 American Society of Civil Engineers.*

Introduction

In many engineering applications, it is desirable or required to characterize the mechanical properties of a semi-infinite medium by means of nondestructive tests. These applications may pertain to deep earth structures, as in exploration geophysics (Mora 1987), or to the near-surface layers, as in the condition evaluation of pavements (Foinquinos 1995; Hadidi and Gucunski 2010) or in geotechnical site characterization (Kallivokas et al. 2013). In nondestructive tests for such applications, the medium is probed with waves (elastic, acoustic, or electromagnetic), the response is recorded, and the distribution of material properties (e.g., shear modulus) is determined by an inversion procedure (Kang and Kallivokas 2011).

For near-surface problems, of interest in this article, the applications that drive most developments to date originate from infrastructure assessment needs. For example, one of the most widely used nondestructive tests for pavement condition assessment is the falling weight deflectometer (FWD) test in which the medium is probed using an impulse load and the response is measured at a number of sensor locations (Fig. 1). Several attempts have been made toward interpretation of FWD test results and extraction of the desired properties of the layered medium. In the context of pavement condition assessment, the property extraction procedures are usually referred to as back-calculations of the relevant properties. In general, back-calculation procedures can be categorized into static and dynamic, on the basis of whether the theoretical response at sensor locations is computed by static analysis or the true dynamic nature of the test is considered. In the static approach, the maximum displacements of the medium at sensor locations are calculated by static elasticity and matched to maximum displacements recorded by sensors. This approach is widely used because of its simplicity and speed, but several studies have shown that static back-calculation results are not reliable (Foinquinos et al. 1995; Maina et al. 2013; Mamlouk 1987; Uzan 1994). In the dynamic approach, the response is calculated via an appropriate forward elastodynamic analysis, and the results are matched to measured displacements. The dynamic forward problem is implemented either in the time (Liu et al. 2007; Loizos and Scarpas 2005) or frequency (Haskell 1953; Thomson 1950) domains. Most frequency-domain procedures (Grenier and Konrad 2009; Yi and Mun 2009; Zhao et al. 2015) are built on the stiffness-matrix formulation introduced by Kausel and Roësset (1981), with further developments by Doyle (1997) and Al-Khoury et al. (2001).

Various techniques have been implemented for the back-calculation of properties (Hadidi and Gucunski 2010). They can be categorized as: (1) closed-form solutions (US Federal Aviation Administration 2004; Hall and Mohseni 1991; Scrivner et al. 1973); (2) database searches (Anderson 1989; Chou and Lytton 1991); (3) optimization techniques (Bush and Alexander 1985; Harichandran et al. 1993; Sivaneswaran et al. 1991); (4) regression analysis (Ali and Khosla 1987; Mahoney et al. 1993; Roque et al. 1998); and (5) neural nets or evolutionary algorithms (Fileccia Scimemi et al. 2016; Meier and Rix 1994, 1995; Rakesh et al. 2006; Saltan et al. 2013; Sharma and Das 2008). Most of the reported techniques are either of an ad hoc nature or resort to simplifying assumptions that are inconsistent with the underlying physical problem (e.g., static versus dynamic).

While progress in the imaging of the near-surface layered media is ongoing, a robust solution remains elusive, possibly because the developed methodologies have not benefited, or have not sought to benefit, from recent advances in related fields. The near-surface imaging problem belongs to a broader class of wave-driven inverse medium problems, where, for example, "back-calculation" refers to, and/or is replaced by, "inversion" (another term that is often used is parameter identification). The tackling of such inverse medium problems is often cast in the context of a partial-differential-equation-constrained optimization framework, whereby a suitably chosen and application-specific objective functional is sought to be

[1]Dept. of Civil, Architectural, and Environmental Engineering, Univ. of Texas at Austin, Austin, TX 78712-0273.

[2]Professor, Dept. of Civil, Architectural, and Environmental Engineering, Univ. of Texas at Austin, Austin, TX 78712-0273 (corresponding author). Email: loukas@mail.utexas.edu

[3]Professor, Dept. of Civil, Architectural, and Environmental Engineering, Univ. of Texas at Austin, Austin, TX 78712-0273.

Note. This manuscript was submitted on May 16, 2017; approved on May 16, 2018; published online on August 25, 2018. Discussion period open until January 25, 2019; separate discussions must be submitted for individual papers. This paper is part of the ***Journal of Engineering Mechanics***, © ASCE, ISSN 0733-9399.

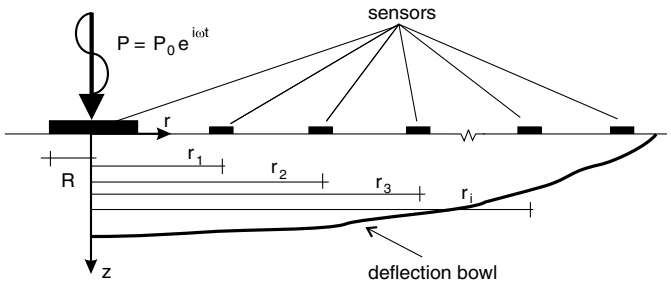

Fig. 1. Schematic drawing of FWD field test: dynamic load, sensor locations, and induced surface deflection bowl.

minimized, constrained by the underlying physics, with the latter expressed in terms of the governing differential equations (Akçelik et al. 2006; Bui-Thanh and Ghattas 2014; Fathi et al. 2015; Kang and Kallivokas 2011; Na and Kallivokas 2008). The technical apparatus for casting and resolving the optimization problem is rooted in the early work of Lions (1971). Such problems, including the one of interest herein, are ill-posed, and typically admit multiple solutions, some physical and some nonphysical. To further narrow the range of possible solutions for the distribution of the properties, several schemes may be used, aimed either at the regularization of the solution, a process that may filter out nonphysical solutions (via, e.g., Tikhonov regularization), or aimed at improving the optimizer's ability to converge to the true (and unique) solution via, possibly physics-based, numerical schemes.

This paper borrows from, and improves upon, recent developments in wave-driven inverse medium problems. Specifically, this article focuses on the problem of a horizontally layered medium subjected to a surface disc load (Fig. 1), and seeks to reconstruct the properties of the layers using the recorded surface displacements. The inverse medium problem is cast as a constrained optimization problem, but instead of using differential equations to describe the underlying physics constraint, the associated eigenvalue problem is used. In principle, any form encompassing the physics of the problem could serve as a constraint (e.g., differential or integral equations). Here, using differential equations as a constraint would result in a two-dimensional problem in either the time or the frequency domain, even under the present conditions of axisymmetry. The motivation for using the eigenvalue problem as a constraint stems from the fact that by using expansions of the displacement in the horizontal directions, which, in turn, give rise to an eigenvalue problem, the spatial dimensionality of the problem is reduced to one, entailing computational gains. Thus, using the eigenvalue problem, i.e., the dispersion relation, appears to be an optimal choice for the problem at hand. In the context of the inverse medium problem of interest herein, using the dispersion relation as a constraint is new; one notable exception where the eigenvalue problem was used as a constraint for shape optimization purposes is the work in Akçelik et al. (2005).

To obtain the associated eigenvalue problem of a semi-infinite layered medium, the forward full-waveform problem is described in the frequency domain, based on the thin-layer method (Kausel 1981): the displacement components in the layered medium are computed using a semidiscrete approach, analytical in all horizontal directions but discrete (numerical) in the medium's depth direction (semi-infinite). To find the property distribution, i.e., to *invert* or *back-calculate*, a stationary point is sought to the problem's Lagrangian, where the latter consists of the misfit between computed and measured responses at various sensor locations, augmented by the imposition of the dispersion relation (eigenvalue problem) and the mode-shape orthonormality conditions. The medium's properties are extracted by enforcing the first-order optimality conditions of the system's Lagrangian. A similar physical problem was considered by Astaneh and Guddati (2016), where the inversion was driven by the misfit between computed and experimentally obtained phase velocities. It is worth noting that the development in Astaneh and Guddati (2016) is intended for inversion on the basis of tests in which surface waves are generated and observed in the far field, while the methodology herein employs arbitrary near-field as well as far-field measurements. The reported numerical results are based on synthetic records, attesting to the effectiveness of the current approach.

Problem Definition

To highlight the dispersion-constrained inversion approach, this article focuses on the simplest possible identification problem, typically associated with the condition assessment of pavements. Accordingly, a horizontally layered medium is considered, comprising n elastic or viscoelastic layers, subjected to a dynamic load applied vertically on the surface of the medium [Fig. 2(a)]. For simplicity, but without loss of generality in the methodology discussed herein, the medium is assumed to be fixed at the bottom. In general, each ith layer is characterized by the shear modulus G_i, Poisson's

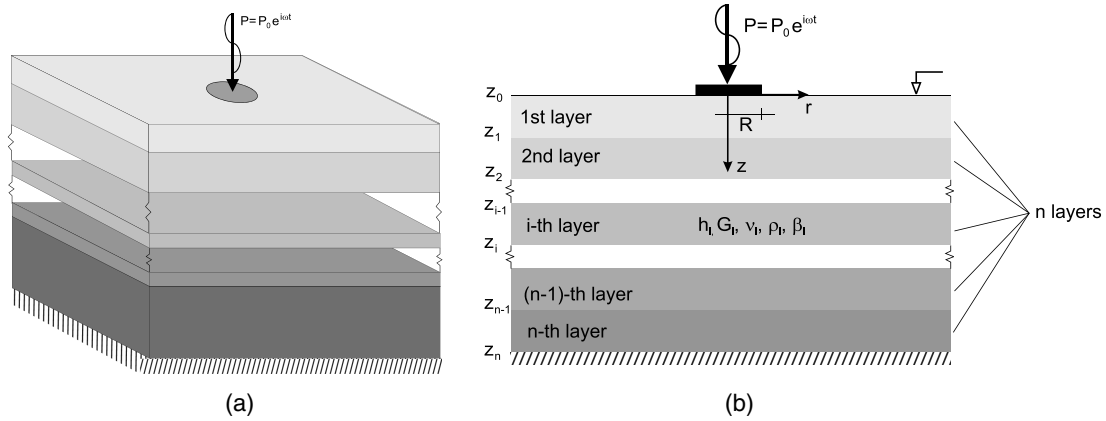

Fig. 2. Layered media subjected to a stationary dynamic load: (a) in three dimensions; and (b) in two dimensions (axisymmetric case).

ratio ν_i, mass density ρ_i, thickness h_i, and material damping β_i. The load is applied normal to the surface at the disc's center: the load is assumed to be harmonic at an operating frequency ω, i.e., $P = P_0 e^{i\omega t}$, where P_0 is the amplitude of the applied load. Given the symmetry of the problem about the vertical load axis, the problem can be formally reduced to an axisymmetric problem cast in the (r, z) system, as shown in Fig. 2(b), where the origin coincides with the disc's center, r denotes radial distance from the origin, and z denotes depth, measured from the surface.

For the purpose of the ensuing discussion, it is assumed that all layer parameters are a priori known, except for the shear moduli and the layer thicknesses, even though, in typical field operations, the layer thicknesses can be obtained by ground penetrating radar (GPR) imaging. Therefore, although the inversion framework can be used to invert for any layer parameters, here, for the sake of simplicity, it is assumed that the density, Poisson's ratio, and damping can be estimated reasonably well from other information, e.g., clayey versus sandy layer, prior to shear-modulus inversion. It should be noted that there is no need to a priori know the number of layers: if the number of layers is known, the inversion process can be further constrained to advantage. However, in the general case, when the number of layers is not known, the number is recovered indirectly, once the shear modulus distribution is obtained. Also, it should be noted that the inverse methodology discussed herein can accommodate additional unknown parameters (e.g., damping), at the expense of increased complexity and computational cost, but without any substantive modification to the inversion framework/algorithm.

Thus, the goal is to recover the shear moduli G_i for all n layers $(i = 1 \ldots n)$, when given the response of the medium to a known excitation, the latter measured at one or multiple surface sensors. The dispersion-constrained approach discussed herein requires that the misfit between the measured displacement and the computed displacement, where the latter corresponds to a trial guess of the layered medium's properties, be minimized. In addition, it is required that the physics of the underlying problem be satisfied: the physics of the problem are expressed in terms of the associated eigenvalue problem, which is used as a minimization constraint—thence the *dispersion-constrained* terminology. The inversion is carried out exclusively in the frequency domain; however, time-domain records can also be used if first processed via Fourier transforms.

Forward Eigenvalue Problem

To set the stage for the dispersion-constrained inversion, first the forward eigenvalue problem should be reviewed; most of the technical details can be found in Kausel (1981). The key steps from Kausel (1981) are reported for completeness.

For any layer i [Fig. 2(b)], the equilibrium equations in cylindrical coordinates and in the frequency domain can be written as (an $e^{i\omega t}$ harmonic term has been assumed throughout):

$$\frac{\partial \tilde{\sigma}_r}{\partial r} + \frac{\tilde{\sigma}_r - \tilde{\sigma}_\theta}{r} + \frac{\partial \tilde{\tau}_{rz}}{\partial z} = -\rho_i \omega^2 \tilde{u} \tag{1a}$$

$$\frac{\partial \tilde{\tau}_{rz}}{\partial r} + \frac{\tilde{\tau}_{rz}}{r} + \frac{\partial \tilde{\sigma}_z}{\partial z} = -\rho_i \omega^2 \tilde{w} \tag{1b}$$

where at the top surface $(z = 0)$:

$$\tilde{\sigma}_z = \begin{cases} q, & 0 \le r \le R \\ 0, & R \le r \end{cases} \tag{2}$$

In Eq. (2), $q = (P_0/\pi R^2)$ is the stress amplitude on the surface when a harmonic load $P_0 e^{i\omega t}$ is applied on the disc of radius R. Due to the axisymmetric character of the problem, the dependence on the polar angle has been dropped, and consequently, the radial component of the displacement $\tilde{u} \equiv \tilde{u}(r, z)$, and the vertical component of the displacement $\tilde{w} \equiv \tilde{w}(r, z)$. Customary notation has been adopted for the Fourier-transformed normal and shear stress components $\tilde{\sigma}_r$, $\tilde{\sigma}_\theta$, $\tilde{\sigma}_z$, $\tilde{\tau}_{rz}$. Similarly, combining the constitutive law for a linear elastic material, and the small-strain kinematic conditions, leads to the equations of motion for the ith layer:

$$(\lambda_i + 2G_i)\left(\frac{\partial^2 \tilde{u}}{\partial r^2} + \frac{1}{r}\frac{\partial \tilde{u}}{\partial r} - \frac{\tilde{u}}{r^2}\right) + G_i \frac{\partial^2 \tilde{u}}{\partial z^2} + (\lambda_i + G_i)\frac{\partial^2 \tilde{w}}{\partial r \partial z} + \rho_i \omega^2 \tilde{u} = 0 \tag{3a}$$

$$(\lambda_i + 2G_i)\frac{\partial^2 \tilde{w}}{\partial z^2} + G_i\left(\frac{\partial^2 \tilde{w}}{\partial r^2} + \frac{1}{r}\frac{\partial \tilde{w}}{\partial r}\right) + (\lambda_i + G_i)\left(\frac{1}{r}\frac{\partial \tilde{u}}{\partial z} + \frac{\partial^2 \tilde{u}}{\partial r \partial z}\right) + \rho_i \omega^2 \tilde{w} = 0 \tag{3b}$$

where λ_i is the first Lamé constant of the ith layer. Using separation of variables and the eigenfunctions, the displacement components can be written as

$$\begin{bmatrix} \tilde{u}(r, z) \\ \tilde{w}(r, z) \end{bmatrix} = \begin{bmatrix} H_1^{(2)}(kr) & 0 \\ 0 & H_0^{(2)}(kr) \end{bmatrix} \begin{bmatrix} u(z) \\ w(z) \end{bmatrix} \tag{4}$$

where k is the wavenumber, $u(z)$ and $w(z)$ are the radial and vertical displacement components, and $H_0^{(2)}(kr)$ and $H_1^{(2)}(kr)$ denote the zero and first order Hankel functions of the second kind, respectively. Introducing Eq. (4) into Eq. (3), results in

$$-k^2(\lambda_i + 2G_i)u + G_i \frac{d^2 u}{dz^2} - k(\lambda_i + G_i)\frac{dw}{dz} + \rho_i \omega^2 u = 0 \tag{5a}$$

$$-k^2 G_i w + (\lambda_i + 2G_i)\frac{d^2 w}{dz^2} + k(\lambda_i + G_i)\frac{du}{dz} + \rho_i \omega^2 w = 0 \tag{5b}$$

The strong form of the forward problem can be cast as follows: find the displacement components (u, w) for each layer i, subject to fixed conditions $(u = w = 0)$ at z_n [Fig. 2(b)], to the continuity of displacements and tractions along the layer interfaces, z_{i-1} and z_i for all i, and to traction-free conditions $(\tilde{\sigma}_z = \tilde{\tau}_{rz} = 0)$ everywhere along the surface $z_0(z = 0)$, except under the load. Next, following a standard Galerkin approach, the weak form for the ith layer, with $z \in (z_{i-1}, z_i)$, becomes

$$k^2(\lambda_i + 2G_i)\int_{z_{i-1}}^{z_i} u\check{u}dz + k\lambda_i \int_{z_{i-1}}^{z_i} \frac{dw}{dz}\check{u}dz - G_i \int_{z_{i-1}}^{z_i} \frac{d}{dz}\left[\frac{du}{dz} - kw\right]\check{u}dz - \rho_i \omega^2 \int_{z_{i-1}}^{z_i} u\check{u}dz = 0 \tag{6a}$$

$$k^2 G_i \int_{z_{i-1}}^{z_i} w\check{w}dz - kG_i \int_{z_{i-1}}^{z_i} \frac{du}{dz}\check{w}dz - \int_{z_{i-1}}^{z_i} \frac{d}{dz}\left[(\lambda_i + 2G_i)\frac{dw}{dz} + k\lambda_i u\right]\check{w}dz - \rho_i \omega^2 \int_{z_{i-1}}^{z_i} w\check{w}dz = 0 \tag{6b}$$

where $\check{u}(z)$ and $\check{w}(z)$ are admissible test functions. After integration by parts, and collecting like terms, the following result:

J. Eng. Mech., 2018, 144(11): 04018099

$$k^2(\lambda_i+2G_i)\int_{z_{i-1}}^{z_i} u\check{u}dz + k\left[\lambda_i\int_{z_{i-1}}^{z_i}\frac{dw}{dz}\check{u}dz - G_i\int_{z_{i-1}}^{z_i} w\frac{d\check{u}}{dz}dz\right] + G_i\int_{z_{i-1}}^{z_i}\frac{du}{dz}\frac{d\check{u}}{dz}dz - \rho_i\omega^2\int_{z_{i-1}}^{z_i} u\check{u}dz = G_i\left[\frac{du}{dz}-kw\right]\check{u}\Big|_{z_{i-1}}^{z_i} = \hat{\tau}_{rz}\check{u}\Big|_{z_{i-1}}^{z_i} \tag{7a}$$

$$k^2G_i\int_{z_{i-1}}^{z_i} w\check{w}dz - k\left[G_i\int_{z_{i-1}}^{z_i}\frac{du}{dz}\check{w}dz - \lambda_i\int_{z_{i-1}}^{z_i} u\frac{d\check{w}}{dz}dz\right] + (\lambda_i+2G_i)\int_{z_{i-1}}^{z_i}\frac{dw}{dz}\frac{d\check{w}}{dz}dz - \rho_i\omega^2\int_{z_{i-1}}^{z_i} w\check{w}dz = \left[(\lambda_i+2G_i)\frac{dw}{dz}+k\lambda_i u\right]\check{w}\Big|_{z_{i-1}}^{z_i} = \hat{\sigma}_z\check{w}\Big|_{z_{i-1}}^{z_i} \tag{7b}$$

where $\hat{\tau}_{rz} = \tilde{\tau}_{rz}/H_1^{(2)}(kr)$ and $\hat{\sigma}_z = \tilde{\sigma}_z/H_0^{(2)}(kr)$. Upon assembly of all the layers, the right-hand sides of Eq. (7) will sum up to zero, due to the continuity and boundary conditions. Next, each layer i is discretized into e_i elements (Fig. 3). The displacement components of the trial pair (u, w) and of the test pair $(\check{u}, \check{w})$ are approximated within each element using standard Lagrange shape functions. Accordingly, within each layer i

$$u(z) = \boldsymbol{\phi}^T(z)\boldsymbol{u}, \qquad w(z) = \boldsymbol{\phi}^T(z)\boldsymbol{w} \tag{8}$$

where $\boldsymbol{u}$ and $\boldsymbol{w}$ are vectors of the nodal values of the radial and vertical displacement components, respectively, and $\boldsymbol{\phi}(z)$ are vectors of shape functions within each layer. For example, if the element shape functions are of polynomial degree d, then the vector $\boldsymbol{\phi}(z)$ has dimension $e_i d + 1$. There results the following quadratic eigenvalue problem in terms of the wavenumber k and the eigenvectors $\boldsymbol{U}$:

$$(k^2\mathbf{A} + k\mathbf{B} + \mathbf{G} - \omega^2\mathbf{M})\boldsymbol{U} = \mathbf{0}; \qquad \boldsymbol{U} = \begin{bmatrix}\boldsymbol{u}\\ \boldsymbol{w}\end{bmatrix} \tag{9}$$

$\mathbf{A}$, $\mathbf{B}$, $\mathbf{G}$ and $\mathbf{M}$ are global matrices assembled using the individual layer matrices, i.e.

$$\mathbf{A} = \bigcup_{i=1}^{n}\mathcal{A}_i; \qquad \mathbf{B} = \bigcup_{i=1}^{n}\mathcal{B}_i; \qquad \mathbf{G} = \bigcup_{i=1}^{n}\mathcal{G}_i; \qquad \mathbf{M} = \bigcup_{i=1}^{n}\mathcal{M}_i \tag{10}$$

where the ith layer matrices $\mathcal{A}_i$, $\mathcal{B}_i$, $\mathcal{G}_i$ and $\mathcal{M}_i$ are defined as

$$\mathcal{A}_i = \begin{bmatrix}(\lambda_i+2G_i)\int_{z_{i-1}}^{z_i}\boldsymbol{\phi}\boldsymbol{\phi}^T dz & 0\\ 0 & G_i\int_{z_{i-1}}^{z_i}\boldsymbol{\phi}\boldsymbol{\phi}^T dz\end{bmatrix},$$

$$\mathcal{B}_i = \begin{bmatrix}0 & \lambda_i\int_{z_{i-1}}^{z_i}\boldsymbol{\phi}\boldsymbol{\phi}'^T dz - G_i\int_{z_{i-1}}^{z_i}\boldsymbol{\phi}'\boldsymbol{\phi}^T dz\\ \lambda_i\int_{z_{i-1}}^{z_i}\boldsymbol{\phi}'\boldsymbol{\phi}^T dz - G_i\int_{z_{i-1}}^{z_i}\boldsymbol{\phi}\boldsymbol{\phi}'^T dz & 0\end{bmatrix},$$

$$\mathcal{G}_i = \begin{bmatrix}G_i\int_{z_{i-1}}^{z_i}\boldsymbol{\phi}'\boldsymbol{\phi}'^T dz & 0\\ 0 & (\lambda_i+2G_i)\int_{z_{i-1}}^{z_i}\boldsymbol{\phi}'\boldsymbol{\phi}'^T dz\end{bmatrix},$$

$$\mathcal{M}_i = \rho_i\begin{bmatrix}\int_{z_{i-1}}^{z_i}\boldsymbol{\phi}\boldsymbol{\phi}^T dz & 0\\ 0 & \int_{z_{i-1}}^{z_i}\boldsymbol{\phi}\boldsymbol{\phi}^T dz\end{bmatrix} \tag{11}$$

Each of the preceding layer matrices has dimension $[2(e_i d+1)] \times [2(e_i d+1)]$. The discrete quadratic eigenvalue problem in Eq. (9) admits $2N$ eigenvalues (the wavenumbers k) and $2N$ eigenvectors (modes), where N is the total number of degrees of freedom, defined as

$$N = \sum_{i=1}^{n} 2e_i d \tag{12}$$

For each wavenumber k, $-k$ is also an eigenvalue; thus, the $2N$ wavenumbers are arranged in N pairs of the form $(k, -k)$. Since the wavenumbers with positive imaginary part correspond to propagating modes that grow away from the origin, only half of the wavenumbers are physically acceptable, i.e., from each pair $(k, -k)$, only the wavenumber with negative imaginary part will be retained. For the N surviving modes, a normalization of the eigenvectors was chosen, similar to the one used by Kausel (1981) and Waas (1972):

$$\frac{1}{2}\boldsymbol{U}_s^T(2k_s\mathbf{A} + \mathbf{B})\boldsymbol{U}_s = k_s, \qquad s = 1, 2, \ldots, N \tag{13}$$

Then, as shown in Kausel (1981), the radial and vertical displacement components within each layer i are given as

$$\tilde{u}(r, z_a) = qR\sum_{s=1}^{N} U_{s,l}U_{s,\frac{N}{2}+1}I_{2s}(r)/k_s \tag{14a}$$

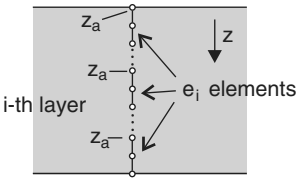

Fig. 3. ith layer discretization into e_i elements.

$$\tilde{w}(r, z_a) = qR \sum_{s=1}^{N} U_{s,m} U_{s,\frac{N}{2}+1} I_{1s}(r) \tag{14b}$$

where s is the eigenmode/eigenvalue index. Within every layer i, the elements are numbered from the top of the layer, with z_a denoting the z coordinate at the beginning of the jth element, with $j = 1, \ldots, e_i$ (Fig. 3). That is

$$z_a = z_{i-1} + (j-1)\frac{z_i - z_{i-1}}{e_i}, \qquad j = 1, \ldots, e_i \tag{15}$$

Thus, in Eq. (14) $U_{s,l}$ and $U_{s,m}$ denote the lth and mth components of the $\boldsymbol{U}_s$ eigenvector, respectively. The $\boldsymbol{U}_s$ eigenvector's components are arranged such that all the $N/2$ radial components are first, followed by the $N/2$ vertical components

$$l = 1 + d(j-1); \qquad m = \frac{N}{2} + 1 + d(j-1) \quad \text{if } i = 1 \tag{16a}$$

$$l = 1 + d(j-1) + \sum_{p=1}^{i-1} e_p d;$$

$$m = \frac{N}{2} + 1 + d(j-1) + \sum_{p=1}^{i-1} e_p d \quad \text{if } i \neq 1 \tag{16b}$$

Furthermore, $I_{1s}(r)$ and $I_{2s}(r)$ in Eq. (14) are defined as

$$I_{1s}(r) = \begin{cases} \dfrac{\pi}{2ik_s} J_0(k_s r) H_1^{(2)}(k_s R) - \dfrac{1}{Rk_s^2}, & 0 \le r \le R \\ \dfrac{\pi}{2ik_s} J_1(k_s R) H_0^{(2)}(k_s r), & R \le r \end{cases} \tag{17a}$$

$$I_{2s}(r) = \begin{cases} \dfrac{\pi}{2i} J_1(k_s r) H_1^{(2)}(k_s R), & 0 \le r \le R \\ \dfrac{\pi}{2i} J_1(k_s R) H_1^{(2)}(k_s r), & R \le r \end{cases} \tag{17b}$$

When the vertical displacements are measured on the surface ($z_a = 0$ or $z = 0$), at a distance r from the load, Eq. (14b) reduces to

$$\tilde{w}(r, 0) = qR \sum_{s=1}^{N} (U_{s,\frac{N}{2}+1})^2 I_{1s}(r) \tag{18}$$

Eq. (18) is used to define the misfit between measured and computed displacements (vertical component only). In summary, it should be noted that the eigenvalue problem in Eq. (9) and the orthonormality condition in Eq. (13) embody the physics of the problem and constitute the forward or state problem: both Eqs. (9) and (13) must be satisfied, as the misfit is minimized. The inversion process is outlined in the next section.

Inverse Problem

Here, the goal is to find the along-the-depth distribution of the shear modulus of the probed layered medium, when the medium is subjected to a known surface disc load. As discussed earlier, it is assumed that the density, Poisson's ratio, and damping are known. Thus, the first Lamé constant, is expressed as a function of the shear modulus G, i.e., $\lambda = [2G\nu/(1-2\nu)]$. Similarly, for viscoelastic layers, G is replaced by its complex counterpart $G(1 + 2i\beta)$.

A usual starting point in inverse-medium problems is the construction of a misfit functional defined most often as the difference, in the least-squares sense, between the measured response and a computed response. The computed response corresponds to a medium described by a set of assumed material properties, which can then be determined via an iterative process whose goal is to minimize the misfit. Accordingly, let $\mathfrak{F}$ denote the misfit functional defined as

$$\mathfrak{F} := \frac{1}{2} \sum_{i=1}^{N_s} \sum_{j=1}^{M_\omega} |\tilde{w}^{(j)}(r_i, 0) - \tilde{w}_m^{(j)}(r_i, 0)|^2 \tag{19}$$

where N_s is the number of sensors, M_ω is the number of discrete frequencies at which sensor measurements are taken, $\tilde{w}^{(j)}(r_i, 0)$ denotes the computed displacement of the layered medium at the jth frequency on the surface and at distance r_i from the origin, and $\tilde{w}_m^{(j)}(r_i, 0)$ denotes the measured displacement at the same point and the same frequency. As cast, the functional in Eq. (19) is the amplitude of the complex-valued misfit, and it is a reasonable choice, since it accounts for both the real and imaginary parts, or equivalently, it includes both amplitude and phase information. Eq. (19) is capable of accounting for recorded data along the deflection bowl induced by the load and over a wide range of excitation frequencies.

To ensure that the physics of the underlying problem is always satisfied during the material inversion iterations, the misfit functional is augmented by the side imposition of the physics to produce the problem's Lagrangian. In general, the side imposition of the physics can be done in a variety of ways: for example, the strong, or a weak, form of the forward problem cast in terms of the governing differential equations, can be side-imposed via Lagrange multipliers. This, in fact, has been a commonly used strategy in partial-differential-equation-constrained optimization approaches for tackling inverse medium problems (Fathi et al. 2015; Kallivokas et al. 2013; Lions 1971). It can be argued that, in principle, any form, continuous or discrete, that faithfully captures the physics of the forward problem, can be used in the Lagrangian. Here, the discrete eigenvalue problem in Eq. (9), accompanied by the orthonormality condition in Eq. (13), is the choice for describing the physics of the problem. Accordingly, Eqs. (9) and (13) are side-imposed, via Lagrange multipliers to the misfit functional, effectively constraining the misfit minimization by the dispersion relation. Thus

$$\mathfrak{L} = \frac{1}{2} \sum_{i=1}^{N_s} \sum_{j=1}^{M_\omega} |\tilde{w}^{(j)}(r_i, 0) - \tilde{w}_m^{(j)}(r_i, 0)|^2 + \mathfrak{C} \tag{20}$$

where $\mathfrak{C}$ is the dispersion constraint defined as

$$\mathfrak{C} = \mathfrak{R}e \left\{ \sum_{j=1}^{M_\omega} \sum_{s=1}^{N} \boldsymbol{\lambda}_s^{(j)T} (\mathbf{A} k_s^{(j)2} + \mathbf{B} k_s^{(j)} + \mathbf{G} - \omega_j^2 \mathbf{M}) \boldsymbol{U}_s^{(j)} + \sum_{j=1}^{M_\omega} \sum_{s=1}^{N} \xi_s^{(j)} \left(\frac{1}{2} \boldsymbol{U}_s^{(j)T} (2\mathbf{A} k_s^{(j)} + \mathbf{B}) \boldsymbol{U}_s^{(j)} - k_s^{(j)} \right) \right\} \tag{21}$$

and $\boldsymbol{\lambda}_s^{(j)}$ is a vector of Lagrange multipliers used to side-impose the eigenvalue problem, and $\xi_s^{(j)}$ is a scalar Lagrange multiplier used for the side-imposition of the orthonormality condition. Since the matrices and eigenvalue parameters are complex, it is sufficient to side-impose only the real part of the product of the complex Lagrange multipliers by the eigenvalue problem and of the orthonormality condition. Next, introducing Eqs. (17) and (18) in the Lagrangian, Eq. (20) becomes

J. Eng. Mech., 2018, 144(11): 04018099

$$\mathfrak{L} = \frac{1}{2}\sum_{i=1}^{N_s}\sum_{j=1}^{M_\omega}\left|qR\sum_{s=1}^{N}\left[\left(U^{(j)}_{s,\frac{N}{2}+1}\right)^2 I^{(j)}_{1s}(r_i)\right] - \tilde{w}^{(j)}_m(r_i,0)\right|^2 + \mathfrak{C} \tag{22}$$

or, equivalently

$$\mathfrak{L} = \begin{cases} \dfrac{1}{2}\displaystyle\sum_{j=1}^{M_\omega}\sum_{i=1}^{N_s}\left|qR\sum_{s=1}^{N}\left[\left(U^{(j)}_{s,\frac{N}{2}+1}\right)^2 \frac{\pi}{2ik^{(j)}_s} J_0(k^{(j)}_s r_i)H^{(2)}_1(k^{(j)}_s R) - \frac{1}{Rk^{(j)2}_s}\right] - \tilde{w}^{(j)}_m(r_i,0)\right|^2 + \mathfrak{C}, & 0 \le r_i \le R \\ \dfrac{1}{2}\displaystyle\sum_{j=1}^{M_\omega}\sum_{i=1}^{N_s}\left|qR\sum_{s=1}^{N}\left[\left(U^{(j)}_{s,\frac{N}{2}+1}\right)^2 \frac{\pi}{2ik^{(j)}_s} J_1(k^{(j)}_s R)H^{(2)}_0(k^{(j)}_s r_i)\right] - \tilde{w}^{(j)}_m(r_i,0)\right|^2 + \mathfrak{C}, & R \le r_i \end{cases} \tag{23}$$

Definitions in Eqs. (22) and (23) of the Lagrangian are of the form

$$\mathfrak{L} \equiv \mathfrak{L}(\boldsymbol{\lambda}^{(j)}_s, \xi^{(j)}_s, \boldsymbol{U}^{(j)}_s, k^{(j)}_s, G_c) \tag{24}$$

i.e., the Lagrangian functional is a function of the Lagrange multipliers $\boldsymbol{\lambda}^{(j)}_s$ and $\xi^{(j)}_s$, the state variables $\boldsymbol{U}^{(j)}_s$ and $k^{(j)}_s$, and the material parameters G_c. The latter are the shear moduli of all the elements in the discretization, assumed constant over each element.

Optimality Conditions

Next, a stationary point for $\mathfrak{L}$ is sought by requiring that the first variations of $\mathfrak{L}$ vanish

$$\nabla\mathfrak{L} = \begin{bmatrix} \delta_{\boldsymbol{\lambda}^{(j)}_s, \xi^{(j)}_s}\mathfrak{L} \\ \delta_{\boldsymbol{U}^{(j)}_s, k^{(j)}_s}\mathfrak{L} \\ \delta_{G_c}\mathfrak{L} \end{bmatrix} = 0 \tag{25}$$

State Problem

Taking variations of the Lagrangian functional $\mathfrak{L}$ with respect to the Lagrange multipliers (or adjoint variables) $\boldsymbol{\lambda}^{(j)}_s$ and $\xi^{(j)}_s$ and setting them equal to zero, recovers the forward eigenvalue problem, i.e., Eqs. (9) and (13)

$$\delta_{\boldsymbol{\lambda}^{(j)}_s}\mathfrak{L} = 0 \Rightarrow (\mathbf{A}_j k^{(j)2}_s + \mathbf{B}k^{(j)}_s + \mathbf{G}_j - \omega^2_j\mathbf{M}_j)\boldsymbol{U}^{(j)}_s = 0 \tag{26a}$$

$$\delta_{\xi^{(j)}_s}\mathfrak{L} = 0 \Rightarrow \frac{1}{2}\boldsymbol{U}^{(j)T}_s(2\mathbf{A}_j k^{(j)}_s + \mathbf{B})\boldsymbol{U}^{(j)}_s = k^{(j)}_s \tag{26b}$$

Adjoint Problem

Similarly, the vanishing of the variation of $\mathfrak{L}$ with respect to the state variables (the wavenumbers $k^{(j)}_s$, and the eigenvectors $\boldsymbol{U}^{(j)}_s$) is enforced. This results in

$$\begin{aligned}\delta_{\boldsymbol{U}^{(j)}_s}\mathfrak{L} = {} & \mathfrak{R}e\left\{2qRU^{(j)}_{s,\frac{N}{2}+1}\sum_{i=1}^{N_s} I^{(j)}_{1s}(r_i)\overline{(\tilde{w}^{(j)}(r_i,0) - \tilde{w}^{(j)}_m(r_i,0))}\boldsymbol{W}^T_I\delta\boldsymbol{U}^{(j)}_s\right\} \\ & + \mathfrak{R}e\left\{\boldsymbol{\lambda}^{(j)T}_s(\mathbf{A}k^{(j)2}_s + \mathbf{B}k^{(j)}_s + \mathbf{G} - \omega^2_j\mathbf{M})\delta\boldsymbol{U}^{(j)}_s + \xi^{(j)}_s\boldsymbol{U}^{(j)T}_s(2\mathbf{A}k^{(j)}_s + \mathbf{B})^T\delta\boldsymbol{U}^{(j)}_s\right\} = 0\end{aligned} \tag{27}$$

or

$$(\mathbf{A}k^{(j)2}_s + \mathbf{B}k^{(j)}_s + \mathbf{G} - \omega^2_j\mathbf{M})^T\boldsymbol{\lambda}^{(j)}_s + (2\mathbf{A}k^{(j)}_s + \mathbf{B})\boldsymbol{U}^{(j)}_s\xi^{(j)}_s = -2qRU^{(j)}_{s,\frac{N}{2}+1}\sum_{i=1}^{N_s} I^{(j)}_{1s}(r_i)\overline{(\tilde{w}^{(j)}(r_i,0) - \tilde{w}^{(j)}_m(r_i,0))}\boldsymbol{W_I} \tag{28}$$

and

$$\delta_{k^{(j)}_s}\mathfrak{L} = \mathfrak{R}e\left\{qR(U^{(j)}_{s,\frac{N}{2}+1})^2\sum_{i=1}^{N_s}\hat{I}^{(j)}_{1s}(r_i)\overline{(\tilde{w}^{(j)}(r_i,0) - \tilde{w}^{(j)}_m(r_i,0))}\delta k^{(j)}_s\right\} + \mathfrak{R}e\left\{\boldsymbol{\lambda}^{(j)T}_s(2\mathbf{A}k^{(j)}_s + \mathbf{B})\boldsymbol{U}^{(j)}_s\delta k^{(j)}_s + \xi^{(j)}_s(\boldsymbol{U}^{(j)T}_s\mathbf{A}\boldsymbol{U}^{(j)}_s - 1)\delta k^{(j)}_s\right\} = 0 \tag{29}$$

or

$$\boldsymbol{U}^{(j)T}_s(2\mathbf{A}k^{(j)}_s + \mathbf{B})^T\boldsymbol{\lambda}^{(j)}_s + (\boldsymbol{U}^{(j)T}_s\mathbf{A}\boldsymbol{U}^{(j)}_s - 1)\xi^{(j)}_s = -qR\left(U^{(j)}_{s,\frac{N}{2}+1}\right)^2\sum_{i=1}^{N_s}\hat{I}^{(j)}_{1s}(r_i)\overline{(\tilde{w}^{(j)}(r_i,0) - \tilde{w}^{(j)}_m(r_i,0))} \tag{30}$$

J. Eng. Mech., 2018, 144(11): 04018099

In the above, $\boldsymbol{W}_I = [0, \ldots 0, 1, 0, \ldots 0]^T$, and

$$\hat{I}_{1s}^{(j)}(r) = \begin{cases} \dfrac{\pi i}{2k_s^{(j)}}[RJ_0(k_s^{(j)}r)H_2^{(2)}(k_s^{(j)}R) + rJ_1(k_s^{(j)}r)H_1^{(2)}(k_s^{(j)}R)] + \dfrac{2}{Rk_s^{(j)3}}, & 0 \le r \le R \\ \dfrac{\pi i}{2k_s^{(j)}}[RJ_2(k_s^{(j)}R)H_0^{(2)}(k_s^{(j)}r) + rJ_1(k_s^{(j)}R)H_1^{(2)}(k_s^{(j)}r)], & R \le r \end{cases} \tag{31}$$

Eqs. (28) and (30) constitute the adjoint problem, which is a symmetric system of $N+1$ linear equations, per

$$\begin{bmatrix} (\mathbf{A}k_s^{(j)2} + \mathbf{B}k_s^{(j)} + \mathbf{G} - \omega_j^2\mathbf{M})^T & (2\mathbf{A}k_s^{(j)} + \mathbf{B})\boldsymbol{U}_s^{(j)} \\ \boldsymbol{U}_s^{(j)T}(2\mathbf{A}k_s^{(j)} + \mathbf{B})^T & (\boldsymbol{U}_s^{(j)T}\mathbf{A}\boldsymbol{U}_s^{(j)} - 1) \end{bmatrix} \begin{bmatrix} \boldsymbol{\lambda}_s^{(j)} \\ \xi_s^{(j)} \end{bmatrix} = \begin{bmatrix} -2qRU_{s,\frac{N}{2}+1}^{(j)}\left(\sum_{i=1}^{N_s} I_{1s}^{(j)}(r_i)(\overline{\tilde{w}^{(j)}(r_i,0) - \tilde{w}_m^{(j)}(r_i,0)})\right)\boldsymbol{W}_I \\ -qR\left(U_{s,\frac{N}{2}+1}^{(j)}\right)^2\left(\sum_{i=1}^{N_s} \hat{I}_{1s}^{(j)}(r_i)(\overline{\tilde{w}^{(j)}(r_i,0) - \tilde{w}_m^{(j)}(r_i,0)})\right) \end{bmatrix} \tag{32}$$

Thus, the Lagrange multipliers, or adjoint variables, $\boldsymbol{\lambda}_s^{(j)}$ and $\xi_s^{(j)}$ are obtained as a solution of the linear system in Eq. (32), which is driven by the (conjugated) misfit, as it can be seen from the right-hand side of Eq. (32).

Control Problem

Lastly, the variation of $\mathfrak{L}$ with respect to the element shear moduli G_c yields

$$\delta_{G_c}\mathfrak{L} = \Re e\left\{\sum_{j=1}^{M_\omega}\sum_{s=1}^{N}\boldsymbol{\lambda}_s^{(j)T}\left(\frac{\partial\mathbf{A}}{\partial G_c}k_s^{(j)2} + \frac{\partial\mathbf{B}}{\partial G_c}k_s^{(j)} + \frac{\partial\mathbf{G}}{\partial G_c}\right)\boldsymbol{U}_s^{(j)} + \sum_{j=1}^{M_\omega}\sum_{s=1}^{N}\xi_s^{(j)}\left(\frac{1}{2}\boldsymbol{U}_s^{(j)T}\left(2\frac{\partial\mathbf{A}}{\partial G_c}k_s^{(j)} + \frac{\partial\mathbf{B}}{\partial G_c}\right)\boldsymbol{U}_s^{(j)}\right)\right\}\delta G_c \tag{33}$$

Clearly, the true/target profile would enforce the vanishing of the control equation, Eq. (33). The right-hand side of Eq. (33), modulo the variation δG_c, represents the reduced gradient of the Lagrangian, since at any given inversion iteration, the state and adjoint problems are satisfied. Thus, from (25), it follows that, at any inversion iteration, there holds

$$\nabla\mathfrak{L} = \begin{bmatrix} 0 \\ 0 \\ \nabla_{G_c}\mathfrak{L} \end{bmatrix} \tag{34}$$

where

$$\nabla_{G_c}\mathfrak{L} = \Re e\left\{\sum_{j=1}^{M_\omega}\sum_{s=1}^{N}\boldsymbol{\lambda}_s^{(j)T}\left(\frac{\partial\mathbf{A}}{\partial G_c}k_s^{(j)2} + \frac{\partial\mathbf{B}}{\partial G_c}k_s^{(j)} + \frac{\partial\mathbf{G}}{\partial G_c}\right)\boldsymbol{U}_s^{(j)} + \sum_{j=1}^{M_\omega}\sum_{s=1}^{N}\xi_s^{(j)}\left(\frac{1}{2}\boldsymbol{U}_s^{(j)T}\left(2\frac{\partial\mathbf{A}}{\partial G_c}k_s^{(j)} + \frac{\partial\mathbf{B}}{\partial G_c}\right)\boldsymbol{U}_s^{(j)}\right)\right\} \tag{35}$$

The reduced gradient $\nabla_{G_c}\mathfrak{L}$, as outlined below, is used to update the shear moduli during the inversion iterations.

Inversion Process

To update/determine the shear moduli G_c, a gradient-based minimization scheme is used. Starting with an assumed initial distribution for the moduli G_c, and a set of M_ω frequencies, solve the state problem in Eqs. (9) and (13), to obtain $k_s^{(j)}$ and $\boldsymbol{U}_s^{(j)}$. Next, using the wavenumbers $k_s^{(j)}$ and the eigenvectors $\boldsymbol{U}_s^{(j)}$, compute the vertical displacement $\tilde{w}^{(j)}$ via Eq. (18), which, in turn, allows the computation of the misfit $\tilde{w}^{(j)} - \tilde{w}_m^{(j)}$ for every sensor for which measurements have been collected. Armed with the misfit and the state variables $(k_s^{(j)}, \boldsymbol{U}_s^{(j)})$, then solve the adjoint problem Eq. (32) for each frequency set to obtain the adjoint variables $\boldsymbol{\lambda}_s^{(j)}$ and $\xi_s^{(j)}$. To update the moduli G_c, use a conjugate gradient approach (Nocedal and Wright 2006), and to ensure sufficient decrease of the objective functional at each inversion iteration, employ an Armijo backtracking line search. Accordingly, let $\boldsymbol{G}_k$ denote the vector of all element moduli G_c and let $\boldsymbol{g}_k = (\nabla_{\boldsymbol{G}}\mathfrak{L})_k$ denote the reduced gradient in eq. (35) of the Lagrangian at the kth inversion iteration. Then, the update $\boldsymbol{G}_{k+1}$ to $\boldsymbol{G}_k$ is constructed via

$$\boldsymbol{G}_{k+1} = \boldsymbol{G}_k + \alpha_k\boldsymbol{S}_k \tag{36}$$

where α_k is a step length, and $\boldsymbol{S}_k$ denotes search direction, defined as

$$\boldsymbol{S}_k = \begin{cases} -\boldsymbol{g}_k, & \text{for } k = 1 \\ -\boldsymbol{g}_k + \dfrac{\boldsymbol{g}_k \cdot \boldsymbol{g}_k}{\boldsymbol{g}_{k-1} \cdot \boldsymbol{g}_{k-1}}\boldsymbol{S}_{k-1}, & \text{for } k > 1 \end{cases} \tag{37}$$

The entire inversion process is summarized in Algorithm 1.

Frequency-Continuation Scheme

As discussed in the Introduction, regularization is often used in inverse medium problems to filter out nonphysical property distributions. In addition to regularizations, other optimizer-assisting schemes are also enlisted; here, one such scheme is chosen, over regularization. Specifically, a frequency-continuation scheme is used, which is consistent with field-deployable equipment capabilities. Accordingly, one can probe the medium at a first set of $M_\omega^{(1)}$ frequencies, whose range is between ω_0 and ω_1, and invert for the properties using Algorithm 1. Once the inversion is concluded, drive the inversion anew using a second set $M_\omega^{(2)}$ of frequencies within, now, the range (ω_0, ω_2) with $\omega_2 > \omega_1$, while using the previously converged profile as initial guess. Note that: (a) the initial range (ω_0, ω_1) is a low-frequency range, aimed at recovering approximately the property profile, since probing with high-frequency content would lead to solutions diverging from the target, as is typically the case with this class of problems; (b) the next set $M_\omega^{(2)}$

contains a few frequencies from $M_\omega^{(1)}$, but also includes higher frequencies, thus allowing refinement of the property profile and the potential discovery of small defects. A small number (5–10) of randomly selected frequencies in each of the probing M_ω sets is sufficient for convergence.

Algorithm 1. Shear moduli inversion scheme
1: Set iteration counter $k \leftarrow 1$
2: Set initial guess for shear moduli $\boldsymbol{G}$
3: Compute misfit $\mathfrak{F} \triangleright$ Eq. (19)
4: Set convergence tolerance *tol*
5: Set maximum number of iterations *maxiter*
6: **while** $\mathfrak{F} > tol$ and $k <$ maxiter **do**
7: Solve the state problem for $k_s^{(j)}$ and $\boldsymbol{U}_s^{(j)} \triangleright$ Eqs. (9) and (13)
8: Solve the adjoint problem for $\boldsymbol{\lambda}_s^{(j)}$ and $\xi_s^{(j)} \triangleright$ Eq. (32)
9: Compute the discrete reduced gradient $\boldsymbol{g}_k \triangleright$ Eq. (35)
10: Compute search direction $\boldsymbol{S}_k \triangleright$ Eq. (37)
11: Choose step length α_k
12: Update material properties and compute $\boldsymbol{G}_{k+1} \triangleright$ Eq. (36)
13: Compute misfit $\mathfrak{F} \triangleright$ Eq. (19)
14: $k \leftarrow k + 1$
15: end while

Numerical Results

To highlight the dispersion-constrained inversion outlined in the previous section, four cases of varying complexity are discussed here, all based on synthetic data. Eq. (23) is used with one sensor for the first 3 cases, with the sensor placed at the center of the disc ($r = 0$), and then Eq. (23) is used with 3 equally spaced sensors for the last case study to demonstrate the capabilities of the process. The first case (Case A) involves a typical heterogeneous layered soil medium with shear moduli monotonically increasing with depth. The second case (Case B) pertains to a layered stratum with an interspersing soft layer between stiffer layers; and for the third case (Case C), a mixed target profile is considered with a stiff but fairly thin layer at the top, which is the typical case for pavements. For the fourth numerical example, Case A is revisited using a 3-sensor array. Finally, to study the performance of the proposed inversion process in the presence of noisy data, Cases A and D are revisited while introducing 5% Gaussian noise to the sensor data. In all cases, to quantify the fitness of the inverted profile with respect to the target, the following normalized L_2 metric is defined:

$$\mathcal{E} = \left[\frac{\int_0^{z_n} (G_e - G_c)^2 dz}{\int_0^{z_n} G_e^2 dz}\right]^{0.5} \tag{38}$$

where G_e denotes the exact shear modulus profile. In all cases, the misfit tolerance *tol* in Algorithm 1 was set to 10^{-10} and the number of maximum inversion iterations *maxiter* was set to 2,000.

Inversion with Noise-Free Data

Case A: Layered Stratum with Monotonically Increasing Moduli

Consider a target layered medium comprising three layers with an overall depth of 2.5 m, where each layer has larger shear modulus than the overlaying layer. The mass density ρ for all layers is set to 1,800 kg/m^3. Poisson's ratio ν is 0.25 for all layers and, a very small damping $\beta = 0.001$ is used. The disc radius is set to $R = 15$ cm. The target shear modulus, and the corresponding shear velocity c_s, profiles are

$$G = \begin{cases} 150 \text{ MPa} & 0 \le z \le 1 \text{ m} \\ 250 \text{ MPa} & 1 \le z \le 1.7 \text{ m} \\ 350 \text{ MPa} & 1.7 \le z \le 2.5 \text{ m} \end{cases}$$

$$c_s \approx \begin{cases} 289 \text{ m/s} & 0 \le z \le 1 \text{ m} \\ 373 \text{ m/s} & 1 \le z \le 1.7 \text{ m} \\ 441 \text{ m/s} & 1.7 \le z \le 2.5 \text{ m} \end{cases}$$

A total of 25 quadratic elements are used to discretize the stratum's depth when inverting for the properties. To create the synthetic data, 52 quadratic elements are used. Note that the mesh used to generate the synthetic data conforms to the physical layer interfaces and consists of elements, which, for any given layer, must and do have identical properties. By contrast, the mesh used for the inversion consists of a different number of elements than those used for the synthetic data. Moreover, these elements do not necessarily conform to the physical layer interfaces, while the individual element properties are set to vary freely. The described meshing differences eliminate any potential biasing of the inversion.

Following the frequency-continuation scheme described earlier, four sets of 10 randomly distributed frequencies are used within each set; the sets are [0, 25] Hz, [0, 50] Hz, [0, 100] Hz, and [0, 150] Hz. One can start the inversion with a homogeneous initial guess of 100 MPa. Fig. 4 shows the inverted profile at the end of the inversion process for each M_ω set. Note that the first set, which has a lower frequency content, constructs an approximate profile starting from a homogeneous initial guess, while the subsequent sets refine the profile as convergence to the target profile is attained. Fig. 5 shows the reduction of misfit across all four frequency sets. For the first frequency set, a drop of about six orders of magnitude in the misfit is seen, seven orders of magnitude for the second frequency set, three orders of magnitude for the third set, and about two orders of magnitude reduction in the fourth frequency set. As shown in Fig. 5, each inversion process consists of 2,000 iterations. The fitness metric after each frequency set is indicative of the progress toward convergence. Overall, the three layers and their interfaces have been satisfactorily recovered, and the final profile is quite close to the target ($\mathcal{E} = 6\%$).

Case B: Layered Stratum with a Soft Layer Trapped between Stiffer Layers

Next, consider a three-layer stratum with $\rho = 1{,}800\,\text{kg/m}^3$, $\nu = 0.25$, $\beta = 0.001$, of an overall depth of 2.5 m, and the following shear modulus target profile and corresponding shear velocity c_s profile:

$$G = \begin{cases} 200 \text{ MPa} & 0 \le z \le 1 \text{ m} \\ 150 \text{ MPa} & 1 \le z \le 1.5 \text{ m} \\ 250 \text{ MPa} & 1.5 \le z \le 2.5 \text{ m} \end{cases}$$

$$c_s \approx \begin{cases} 333 \text{ m/s} & 0 \le z \le 1 \text{ m} \\ 289 \text{ m/s} & 1 \le z \le 1.5 \text{ m} \\ 373 \text{ m/s} & 1.5 \le z \le 2.5 \text{ m} \end{cases}$$

Again, 52 quadratic elements are used for the synthetic data, and 25 quadratic elements for the inversion, and the same frequency continuation scheme as in Case A. Note that there is a thin layer at $1 \le z \le 1.5$ m, which has a smaller shear modulus in comparison with the adjacent layers. Fig. 6 shows the inverted profile at the end of the inversion process for each M_ω set. Note that the reconstruction is quite satisfactory even in this case where the

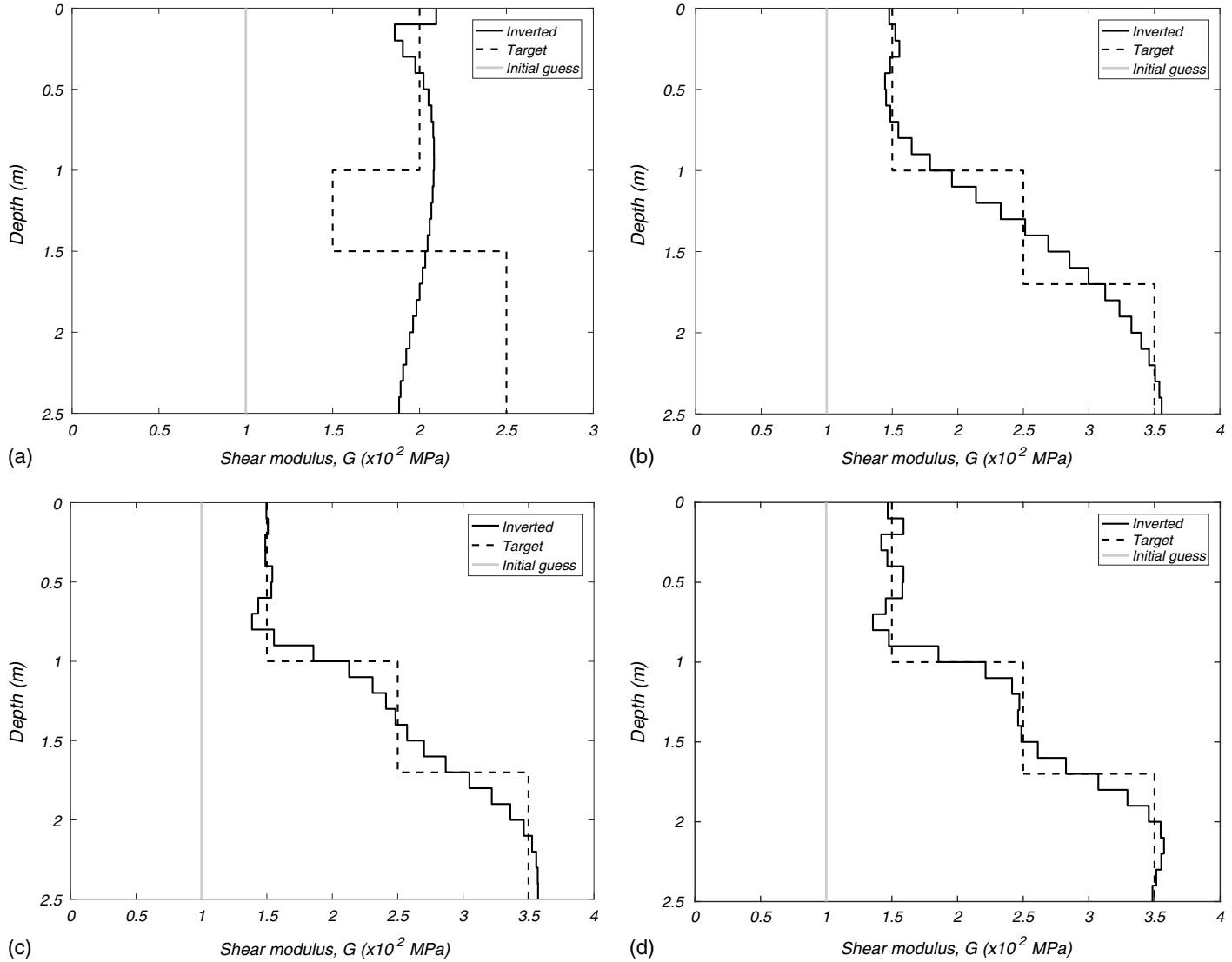

Fig. 4. Case A: target and inverted shear modulus profiles shown at the end of the inversion process for each frequency set M_ω, with fitness metric $\mathcal{E}$: (a) $M_\omega^{(1)}$, $\mathcal{E} = 35\%$; (b) $M_\omega^{(2)}$, $\mathcal{E} = 8.5\%$; (c) $M_\omega^{(3)}$, $\mathcal{E} = 7.1\%$; and (d) $M_\omega^{(4)}$, $\mathcal{E} = 6\%$.

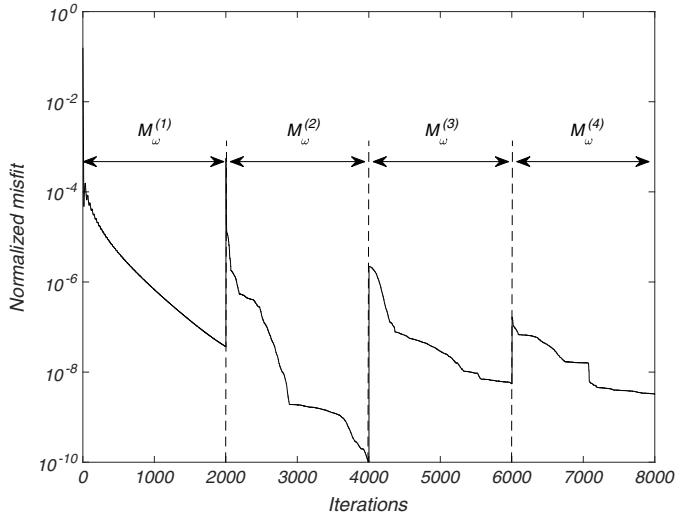

Fig. 5. Case A—Misfit reduction for all frequency sets M_ω.

presence of the soft layer tends to mask the deeper stratum structure, due to its trapped energy potential. The associated fitness metric was $\mathcal{E} = 4.8\%$.

Case C: Thin Top Layer: Typical Pavement Structure

Next, a medium comprising four layers is considered, where the top layer is rather thin and stiff (a reasonable approximation for pavements). The target profile is

$$G = \begin{cases} 1{,}000 \text{ MPa} & 0 \le z \le 0.2 \text{ m} \\ 400 \text{ MPa} & 0.2 \le z \le 0.6 \text{ m} \\ 300 \text{ MPa} & 0.6 \le z \le 1 \text{ m} \\ 500 \text{ MPa} & 1 \le z \le 2 \text{ m} \end{cases}$$

$$c_s \approx \begin{cases} 745 \text{ m/s} & 0 \le z \le 0.2 \text{ m} \\ 471 \text{ m/s} & 0.2 \le z \le 0.6 \text{ m} \\ 408 \text{ m/s} & 0.6 \le z \le 1 \text{ m} \\ 527 \text{ m/s} & 1 \le z \le 2 \text{ m} \end{cases}$$

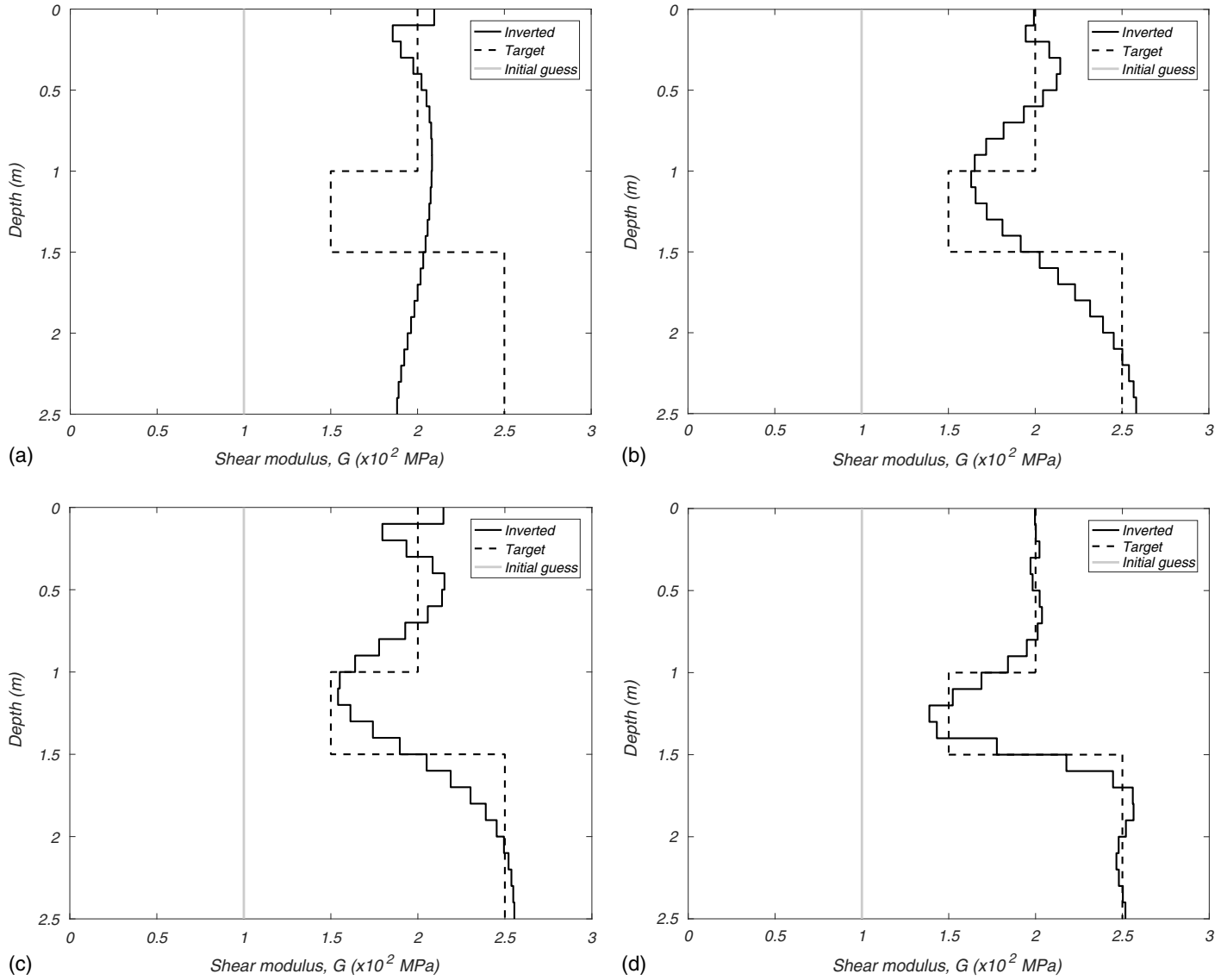

Fig. 6. Case B: target and inverted shear modulus profiles shown at the end of the inversion process for each frequency set M_ω, with fitness metric $\mathcal{E}$: (a) $M_\omega^{(1)}$, $\mathcal{E} = 20\%$; (b) $M_\omega^{(2)}$, $\mathcal{E} = 10\%$; (c) $M_\omega^{(3)}$, $\mathcal{E} = 8\%$; and (d) $M_\omega^{(4)}$, $\mathcal{E} = 4.8\%$.

Again, 52 quadratic elements are used for the synthetic data, and 25 quadratic elements for inversion. The same frequency continuation scheme is used as in the preceding cases. The inverted profiles for each frequency set are shown in Fig. 7.

Despite the thinness of the top layer and the sharp contrast (jump) in the shear moduli between the top and second layers, the inversion process has again quite satisfactorily recovered the target, with a fitness of $\mathcal{E} = 6.2\%$.

Case D: Case A Revisited with a 3-Sensor Array

Again Case A is considered, with the same profile and mesh properties as previously described. For the inversion process, Eq. (23) is used with $N_s = 3$ to solve the inverse medium problem: synthetically measured and computed displacements are recorded at three sensor locations, namely at $r = 0$, $r = 30$ cm and $r = 60$ cm. That is, the first sensor is under the load, whereas the other two are along the surface of the stratum. As in the preceding cases, the frequency-continuation scheme is used to drive the inversion with the same probing frequency sets as of Case A. Fig. 8 shows the inverted shear modulus profile. The result shows a good match between the inverted shear modulus profile and the target profile with the fitness metric $\mathcal{E} = 4.4\%$, an improvement over the single sensor case ($\mathcal{E} = 6\%$).

Inversion with Noisy Data

Here, a 5% Gaussian noise is applied to the synthetic sensor data used for Cases A and D, and then inversion for the layer moduli is attempted. In each case, to generate the noisy data, the synthetic complex displacements over all frequency sets are treated as a (power) signal; a 5% background noise is assumed, and the signal-to-noise ratio (SNR $\simeq$ 13 dB) is computed. The synthetic data and the SNR are fed to MATLAB'S awgn function (Gaussian noise) to generate the noisy data. The resulting noisy displacement amplitudes varied between 0.05% and 4.4% of the unperturbed synthetic data.

Case E: Case A with Noisy Data

Case A is considered with the same profile and mesh properties as used in Case A. The same set of frequencies and frequency-continuation scheme are used for the inversion (Fig. 11). Similar to Case A, the inverted shear modulus profile at the end of each

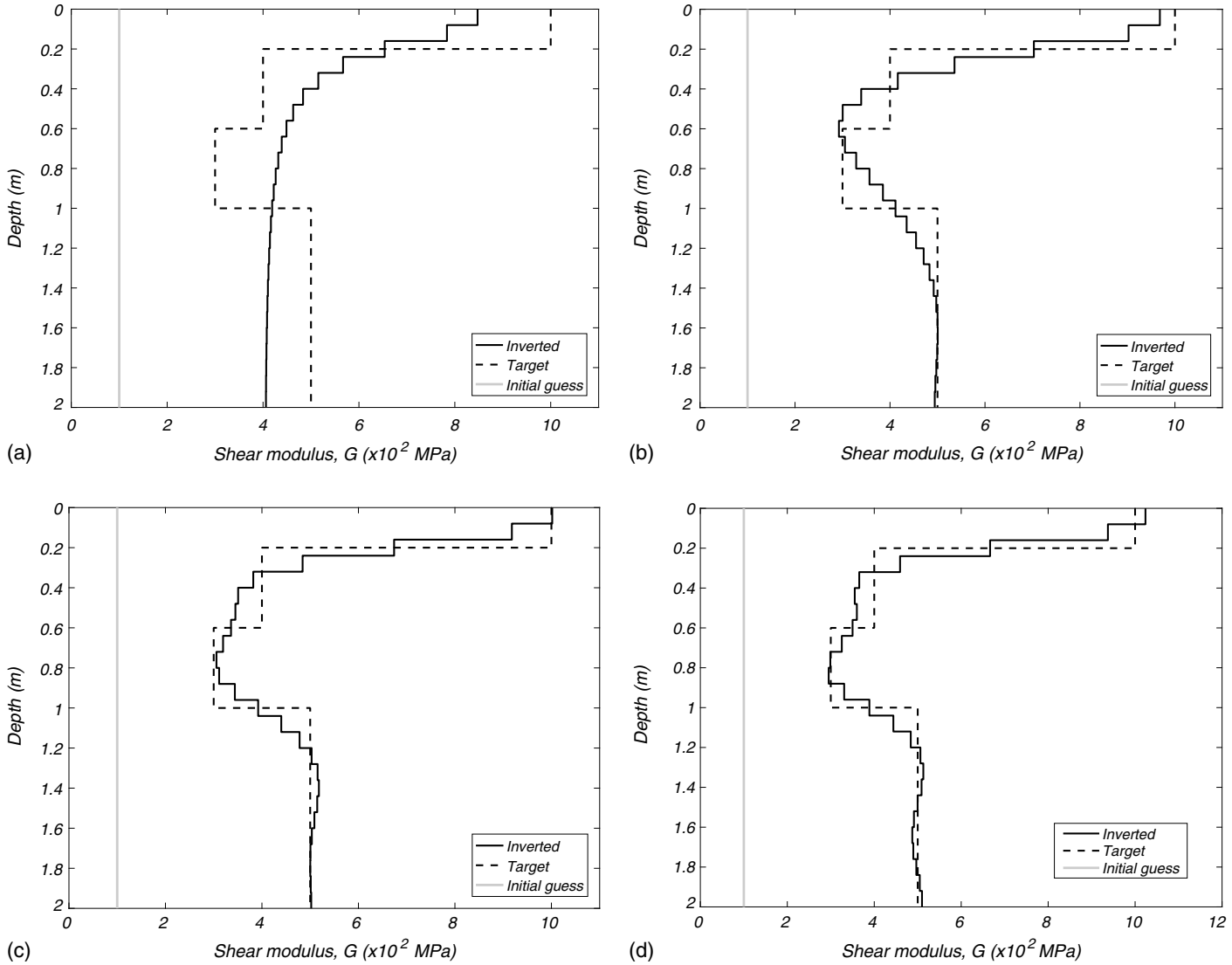

Fig. 7. Case C: target and inverted shear modulus profiles shown at the end of the inversion process for each frequency set M_ω, with fitness metric $\mathcal{E}$: (a) $M_\omega^{(1)}$, $\mathcal{E} = 24\%$; (b) $M_\omega^{(2)}$, $\mathcal{E} = 15\%$; (c) $M_\omega^{(3)}$, $\mathcal{E} = 9.4\%$; and (d) $M_\omega^{(4)}$, $\mathcal{E} = 6.2\%$.

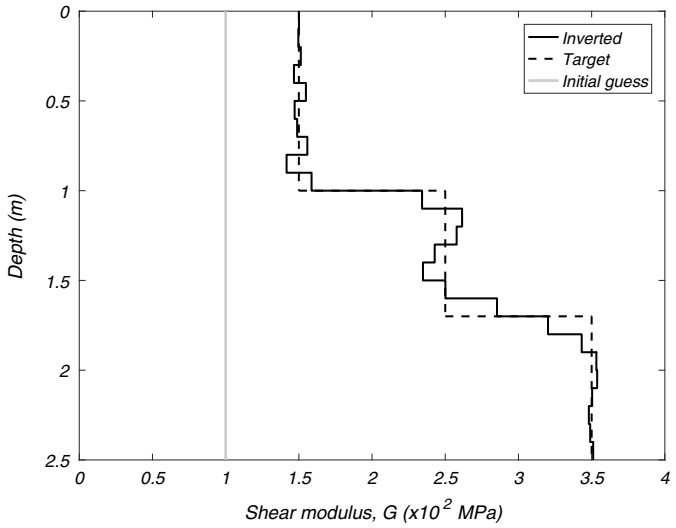

Fig. 8. Case D: inverted shear modulus profile of Case A with a 3-sensor array.

frequency set and corresponding fitness metric is shown in Fig. 9. Despite the increase in the fitness metric, the inverted profile represents the target profile satisfactorily. Three different layers are distinguishable and the shear modulus of each layer has been recovered. Comparing with Case A, adding 5% noise to the data results in change of fitness metric from 6% to 9.6%. Fig. 10 shows the reduction of the misfit through the inversion for each frequency set. Due to the applied noise, the reduction in the order of misfit at each frequency set is smaller than in Case A (Fig. 5). Fig. 11 shows the noisy sensor data for all frequencies used for the inversion. More interestingly, Fig. 11 depicts the frequency response curves one would obtain using the target profile, the profile inverted using noise-free data, and the profile inverted using noisy data. As can be seen, all frequency response curves are fairly close. Note that the frequency response curve obtained for the noisy data case departs the most from the corresponding sensor data points, as also evidenced by the relatively large misfit values.

Note that, in the absence of regularization, the inversion process could yield nonphysical profiles that match the data (noisy or noise-free). In Case E, though, the inversion process resulted in a profile that matches closely the target, in the presence of noisy data and in

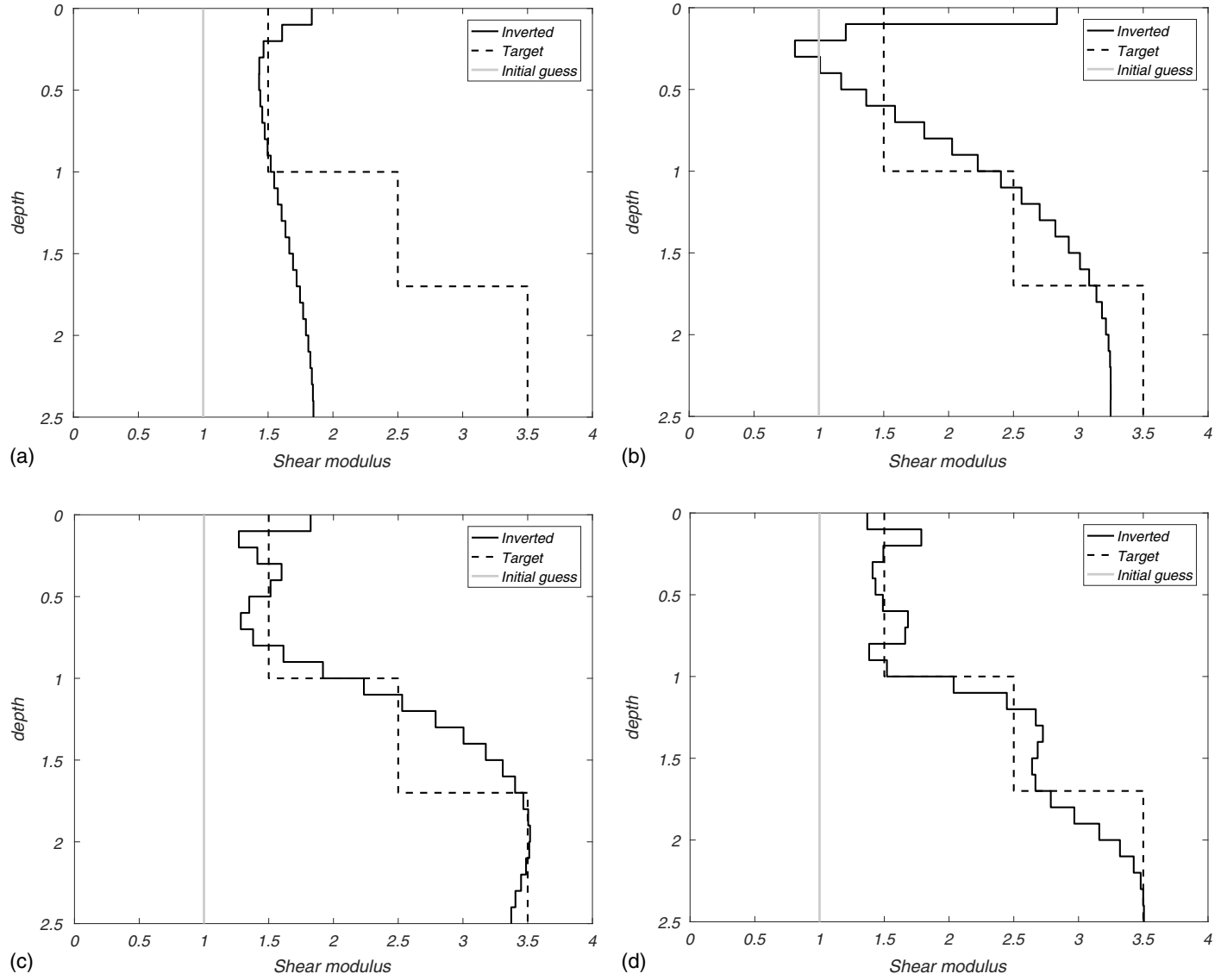

Fig. 9. Case E: target and inverted shear modulus profiles shown at the end of the inversion process for each frequency set M_ω, with fitness metric $\mathcal{E}$ (noisy-data): (a) $M_\omega^{(1)}$, $\mathcal{E} = 41\%$; (b) $M_\omega^{(2)}$, $\mathcal{E} = 17.6\%$; (c) $M_\omega^{(3)}$, $\mathcal{E} = 13.1\%$; and (d) $M_\omega^{(4)}$, $\mathcal{E} = 9.6\%$.

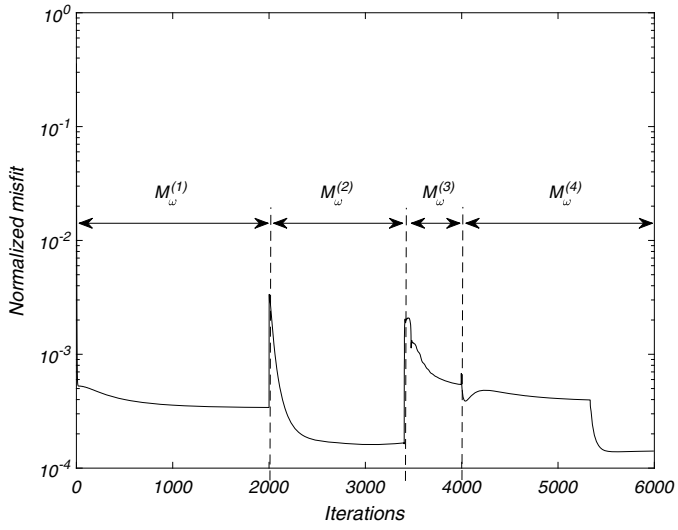

Fig. 10. Case E—Misfit reduction for each frequency set M_ω.

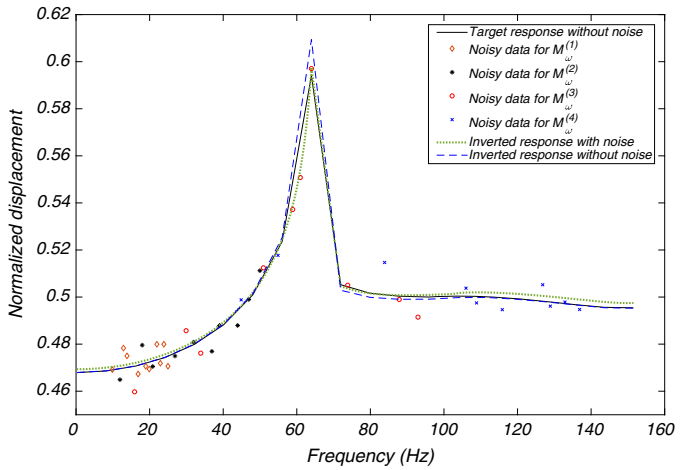

Fig. 11. Frequency responses of the target profile for Cases A and E, of the inverted profile with noise-free data and of the inverted profile with noisy data, along with the sensor data used for each frequency set.

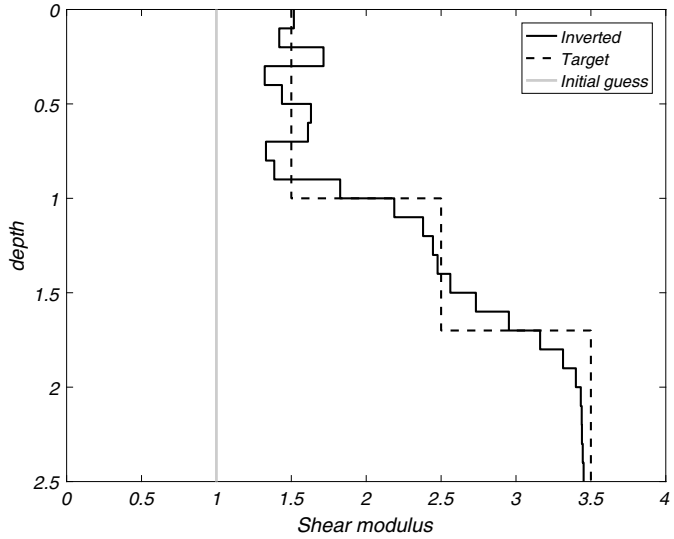

Fig. 12. Case F: inverted shear modulus profile of Case A with a 3-sensor array and 5% added noise.

the absence of regularization. Note that a frequency response curve that would have closely matched the noisy data (with a misfit value similar to Case A), would have had to be fairly oscillatory in the low-frequency regime. Such a frequency response would correspond to a profile that is not recoverable by the relatively coarse mesh we are using. Thus, it can be conjectured that, in effect, the coarseness of the mesh has, in this case, acted as a regularizer. In general, regularization would be required to alleviate solution multiplicity.

Case F: Case D with Noisy Data

Next, Case D is considered with the same profile and mesh properties as earlier, i.e., 25 quadratic elements are used along the depth. Measured and computed displacements are recorded at three sensors: $r = 0$, $r = 30$ cm, and $r = 60$ cm. The synthetically measured displacements are polluted with 5% Gaussian noise and then used for the inversion process. The inverted shear modulus profile is shown in Fig. 12. Comparing with Case D, the fitness metric has increased from 4.4% to 7% due to the added noise. Despite the noise, the inverted profile matches the target reasonably well. Comparing with Case E, the use of three sensors, instead of one, has resulted in an improved fitness metric of 7% versus 9.6%.

Conclusion

This paper discussed a new dispersion-constrained optimization approach for resolving the inverse medium problem associated with the reconstruction of the material profile of a layered medium, based on surface measurements of its response to surface excitation. The methodology imposes the forward eigenvalue problem, provided by the thin-layer method, as a side constraint to a misfit functional to form the inversion problem's Lagrangian. This facilitates the iterations toward minimization of the misfit. Other key advantages of the methodology include: (1) use is made of the complete recorded displacement waveforms, whether in the near-field or the far-field, without need for any simplifying assumptions; and (2) spatial discretization is needed only in one dimension. The methodology accommodates single or multiple sensor measurements, and takes advantage of the frequency agility of typical wave generating field equipment to embed, to advantage, a frequency-continuation scheme within the inversion problem.

The reported numerical results attest to the method's ability to invert for the moduli, and indirectly for the thicknesses, of a layered medium. Apart from demonstrating successful inversions of shear-modulus profiles using measurements from a single sensor, it was also shown that increasing the number of sensors in the inversion process will lead to improvements in the inverted profiles. Therefore, the methodology is highly promising in applications to pavement testing where data from multiple sensors are routinely recorded. Furthermore, the computational experiments indicate that the methodology is capable of recovering the material parameters satisfactorily in the presence of noise in the recorded displacement data.

References

Akçelik, V., G. Biros, O. Ghattas, J. Hill, D. Keyes, and B. van Bloemen Waanders. 2006. "Parallel algorithms for PDE-constrained optimization." In *Parallel processing for scientific computing*, edited by M. Heroux, P. Raghavan, and H. Simon, 291–322. Philadelphia: SIAM.

Akçelik, V., G. Biros, O. Ghattas, D. Keyes, K. Ko, L. Lee, and E. Ng. 2005. "Adjoint methods for electromagnetic shape optimization of the low-loss cavity for the international linear collider." *J. Phys.: Conf. Ser.* 16 (1): 435–445.

Ali, N., and N. Khosla. 1987. "Determination of layer moduli using a falling weight deflectometer." *Transp. Res. Rec.* 1117: 1–10.

Al-Khoury, R., C. Kasbergen, A. Scarpas, and J. Blaauwendraad. 2001. "Spectral element technique for efficient parameter identification of layered media." *Int. J. Solids Struct.* 38 (48): 8753–8772. https://doi.org/10.1016/S0020-7683(01)00109-3.

Anderson, M. 1989. "A data base method for backcalculation of composite pavement layer moduli." In Vol. 1026 of *Nondestructive testing of pavements and backcalculation of moduli*, 201–216. West Conshohocken, PA: ASTM.

Astaneh, A., and M. Guddati. 2016. "Improved inversion algorithms for near-surface characterization." *Geophys. J. Int.* 206 (2): 1410–1423. https://doi.org/10.1093/gji/ggw192.

Bui-Thanh, T., and O. Ghattas. 2014. "A PDE-constrained optimization approach to the discontinuous Petrov-Galerkin method with a trust region inexact Newton-CG solver." *Comput. Methods Appl. Mech. Eng.* 278: 20–40. https://doi.org/10.1016/j.cma.2014.04.018.

Bush, A., and D. Alexander. 1985. "Pavement evaluation using deflection basin movement and layered theory." *Transp. Res. Rec.* 1022: 16–29.

Chou, Y., and R. Lytton. 1991. "Accuracy and consistency of backcalculated pavement layer moduli." *Transp. Res. Rec.* 1293: 72–85.

Doyle, J. F. 1997. *Wave propagation in structures: Spectral analysis using fast discrete Fourier transforms*. 2nd ed. New York: Springer.

Fathi, A., L. F. Kallivokas, and B. Poursartip. 2015. "Full-waveform inversion in three-dimensional PML-truncated elastic media." *Comput. Methods Appl. Mech. Eng.* 296: 39–72. https://doi.org/10.1016/j.cma.2015.07.008.

Fileccia Scimemi, G., T. Turetta, and C. Celauro. 2016. "Backcalculation of airport pavement moduli and thickness using the Lévy Ant Colony optimization algorithm." *Constr. Build. Mater.* 119: 288–295. https://doi.org/10.1016/j.conbuildmat.2016.05.072.

Foinquinos, R. 1995. "Dynamic nondestructive testing of pavements." Ph.D. dissertation, Dept. of Civil Engineering, Univ. of Texas at Austin.

Foinquinos, R., J. Roësset, and K. Stokoe. 1995. "Response of pavement systems to dynamic loads imposed by nondestructive tests." *Transp. Res. Rec.* 1504: 57–67.

Grenier, S., and J. Konrad. 2009. "Dynamic interpretation of falling weight deflectometer tests on flexible pavements using the spectral element method: backcalculation." *Can. J. Civ. Eng.* 36 (6): 957–968. https://doi.org/10.1139/L09-010.

Hadidi, R., and N. Gucunski. 2010. "Comparative study of static and dynamic falling weight deflectometer back-calculations using probabilistic approach." *J. Transp. Eng.* 136 (3): 196–204. https://doi.org/10.1061/(ASCE)0733-947X(2010)136:3(196).

Hall, K., and A. Mohseni. 1991. "Backcalculation of asphalt concrete-overlaid portland cement concrete pavement layer moduli." *Transp. Res. Rec.* 1293: 112–123.

Harichandran, R., T. Mahmood, A. Raab, and G. Baladi. 1993. "Modified Newton algorithm for backcalculation of pavement layer properties." *Transp. Res. Rec.* 1384: 15–22.

Haskell, N. A. 1953. "The dispersion of surface waves on multilayered media." *Bull. Seismol. Soc. Am.* 43 (1): 17–34. https://doi.org/10.1029/SP030p0086.

Kallivokas, L. F., A. Fathi, S. Kucukcoban, K. Stokoe, J. Bielak, and O. Ghattas. 2013. "Site characterization using full waveform inversion." *Soil Dyn. Earthquake Eng.* 47: 62–82. https://doi.org/10.1016/j.soildyn.2012.12.012.

Kang, J., and L. Kallivokas. 2011. "The inverse medium problem in heterogeneous PML-truncated domains using scalar probing waves." *Comput. Methods Appl. Mech. Eng.* 200 (1–4): 265–283. https://doi.org/10.1016/j.cma.2010.08.010.

Kausel, E. 1981. *An explicit solution for the green functions for dynamic loads in layered media*. Cambridge, MA: Massachusetts Institute of Technology.

Kausel, E., and J. Roësset. 1981. "Stiffness matrices for layered soils." *Bull. Seismol. Soc. Am.* 71 (6): 1743–1761. https://doi.org/10.1016/0148-9062(83)91665-0.

Lions, J. L. 1971. Vol. Bd. 170 of *Optimal control of systems governed by partial differential equations*. New York: Springer.

Liu, M., H. Liao, and J. Chuang. 2007. "Dynamic time domain back-calculation of LTPP test sites." *J. Eastern Asia Soc. Transp. Stud.* 7: 2017–2029.

Loizos, A., and J. Scarpas. 2005. "Verification of falling weight deflectometer backanalysis using a dynamic finite elements simulation." *Int. J. Pavement Eng.* 6 (2): 115–123. https://doi.org/10.1080/10298430500141030.

Mahoney, J., B. Winters, N. Jackson, and L. Pierce. 1993. "Some observations about backcalculation and use of a stiff layer condition." *Transp. Res. Rec.* 1384: 8–14.

Maina, J., W. Steyn, E. van Wyk, and F. le Roux. 2013. "Static and dynamic backcalculation analyses of an inverted pavement structure." Vol. 723 of *Innovation and sustainable technology in road and airfield pavement: Advanced materials research*, 196–203. Portland, OR: Trans Tech Publications.

Mamlouk, M. S. 1987. "Dynamic analysis of multilayered pavement structures—Theory, significance and verification." In *Proc., 6th Int. Conf. on Structural Design of Asphalt Pavements*, 466–473. Ann Arbor, MI: Cushing-Malloy, Inc.

Meier, R., and G. Rix. 1994. "Backcalculation of flexible pavement moduli using artificial neural networks." *Transp. Res. Rec.* 1448: 75–82.

Meier, R., and G. Rix. 1995. "Backcalculation of flexible pavement moduli from dynamic deflection basins using artificial neural networks." *Transp. Res. Rec.* 1473: 72–81.

Mora, P. 1987. "Nonlinear two-dimensional elastic inversion of multioffset seismic data." *Geophysics* 52 (9): 1211–1228. https://doi.org/10.1190/1.1442384.

Na, S.-W., and L. F. Kallivokas. 2008. "Partial-differential-equation-constrained amplitude-based shape detection in inverse acoustic scattering." *Comput. Mech.* 41 (4): 579–594. https://doi.org/10.1007/s00466-007-0216-4.

Nocedal, J., and S. J. Wright. 2006. *Numerical optimization*. 2nd ed. New York: Springer.

Rakesh, N., A. K. Jain, M. A. Reddy, and K. S. Reddy. 2006. "Artificial neural networks-genetic algorithm based model for backcalculation of pavement layer moduli." *Int. J. Pavement Eng.* 7 (3): 221–230. https://doi.org/10.1080/10298430500495113.

Roque, R., B. Ruth, and S. Sedwick. 1998. "Limitations of backcalculation and improved methods for pavement layer moduli predictions." In *Proc., 5th Int. Conf. on the Bearing Capacity of Roads and Airfields*. Trondheim, Norway: Tapir Publishing.

Saltan, M., V. Uz, and B. Aktas. 2013. "Artificial neural networks-based backcalculation of the structural properties of a typical flexible pavement." *Neural Comput. Appl.* 23 (6): 1703–1710. https://doi.org/10.1007/s00521-012-1131-y.

Scrivner, F., C. Michalak, and W. Moore. 1973. "Calculation of the elastic moduli of a two-layer pavement system from measured surface deflections." *Highway Res. Rec.* 431: 12–24.

Sharma, S., and A. Das. 2008. "Backcalculation of pavement layer moduli from falling weight deflectometer data using an artificial neural network." *Can. J. Civ. Eng.* 35 (1): 57–66. https://doi.org/10.1139/L07-083.

Sivaneswaran, N., S. Kramer, and J. Mahoney. 1991. "Advanced back-calculation using a nonlinear least squares optimization technique." *Transp. Res. Rec.* 1293: 93–102.

Thomson, W. T. 1950. "Transmission of elastic waves through a stratified solid medium." *J. Appl. Phys.* 21 (2): 89–93. https://doi.org/10.1063/1.1699629.

US Federal Aviation Administration. 2004. *Use of nondestructive testing in the evaluation of airport pavements*. Washington, DC: US Dept. of Transportation, Federal Aviation Administration.

Uzan, J. 1994. "Advanced backcalculation techniques." In Vol. 1198 of *Nondestructive testing of pavement and backcalculation of moduli*. 3–37. West Conshohocken, PA: ASTM.

Waas, G. 1972. "Linear two-dimensional analysis of soil dynamics problems in semi-infinite layered media." Ph.D. dissertation, Dept. of Civil Engineering, Univ. of California, Berkeley.

Yi, J., and S. Mun. 2009. "Backcalculating pavement structural properties using a Nelder-Mead simplex search." *Int. J. Numer. Anal. Methods Geomech.* 33 (11): 1389–1406. https://doi.org/10.1002/nag.769.

Zhao, Y., D. Cao, and P. Chen. 2015. "Dynamic backcalculation of asphalt pavement layer properties using spectral element method." *Road Mater. Pavement Des.* 16 (4): 870–888. https://doi.org/10.1080/14680629.2015.1056214.